Electronic Supplementary Material (ESI) for Energy & Environmental Science.

Supporting Information

Restrained Energetic Disorder for High-Efficiency Organic Solar Cells via a Solid Additive

Zhihao Chen,[1] Huifeng Yao,[1,*] Jingwen Wang,[1,2] Jianqi Zhang,[3] Tao Zhang,[1,2] Zi Li,[1] Jiawei Qiao,[4] Shishuai Xiu,[2] Xiaotao Hao,[4] and Jianhui Hou[1,2,*]

[1]State Key Laboratory of Polymer Physics and Chemistry, Beijing National Laboratory for Molecular Sciences, Institute of Chemistry, Chinese Academy of Sciences, Beijing 100190, China.
[2]University of Chinese Academy of Sciences, Beijing 100049, China.
[3]Key Laboratory of Nanosystem and Hierarchical Fabrication, National Center for Nanoscience and Technology, Beijing, 100190, China.
[4]School of Physics, State Key Laboratory of Crystal Materials, Shandong University, Jinan, 250100, China

Materials

PBDB-TF, eC9, HDO-4Cl, PBQx-TF, eC9-2Cl, Y6, and PDINN were purchased from Solarmer Material Inc. TMB was purchased from Merck Inc. PEDOT:PSS (clevios P VP Al 4083) was purchased from H.C. Starck co.

Calculation

The optimal geometries were optimized by Gaussian 09 at the level of B3LYP/6-31G(d,p).[1] The long alkyl chains were replaced by methyl group or 3-isobutyl groups to save time. The excited states were calculated by time-dependent DFT on CAM-B3LYP/6-31G (d, p) level. The excited state analysis[2] and the IGMH analysis[3] were performed by Multiwfn.[4]

Device fabrication

The patterned Indium tin oxide (ITO) coated glass substrates were procured from South China Xiang's Science & Technical Company Limited. The ITO substrates underwent a sequential cleaning process, consisting of 20-minute treatments in detergent, de-ionized water, acetone, and ethanol, respectively. The cleaned ITO substrates were further subjected to an oxygen plasma treatment for 30 minutes. PEDOT:PSS thin films, with a thickness of approximately 15 nm, were spin-coated onto the cleaned substrates, and then annealed for 15 minutes at 150°C in air environment. Subsequently, blend solutions were spin-coated onto the PEDOT:PSS layers, in which PBDB-TF:eC9 and PBDB-TF:Y6 (D:A = 1:1.2) were dissolved in chloroform at a polymer concentration of 7 mg ml^{-1}, PBQx-TF:eC9-2Cl (1:1.2) was dissolved in toluene at a polymer concentration of 6.5 mg ml^{-1}, PBDB-TF:IT-4F (1:1) was dissolved in chlorobenzene at a polymer concentration of 7 mg ml^{-1}, and PBDB-TF:eC9:HDO-4Cl (1:1:0.2) was dissolved in chloroform at a polymer concentration of 7 mg ml^{-1}. The DIO and CN additives were incorporated at an optimal volume percentage of 0.5 vol%, while the TMB additive was incorporated at an optimal concentration of 10 mg ml^{-1}. The DIO and CN treated films were annealed at 100°C for 10 minutes, while the TMB treated films were annealed at 100°C for 5 minutes. Subsequently, PDINN layers with a thickness of approximately 5 nm were spin-coated onto the active layers. Finally, 100 nm thick Ag layers were thermally evaporated through shadow masks to complete the fabrication of the devices. The device contact area is 0.09 cm^2. The areas of the masks are about

0.0617 cm^2.

Instruments and characteristics

Photoelectric characteristics

The current-voltage (*J-V*) characteristics were measured using a Keithley 2400 under AM 1.5G illumination at an intensity of 100 mW cm^{-2} (XES-70S1, SAN-EI Electric Co., Ltd.). The *J-V* scan speed is 0.02 V s^{-1} and a dwell time of 5 ms. The light intensity was calibrated using a certified standard silicon solar cell (SRC-2020, 174 Enlitech). The external quantum efficiency (EQE) spectra were measured using the Solar Cell Spectral Response Measurement System QE-R3011 (Enli Technology Co., Ltd., Taiwan). The photo-CELIV measurements were conducted using the all-in-one characterization platform Paios, developed and commercialized by Fluxim AG, Switzerland. To ensure accurate results, all devices were prepared for photo-CELIV measurements in accordance with the relevant device fabrication conditions. The ramp rate was set at 0.10 V/us, the delay time was 70 us, the light pulse length was 30 us, and the setup-type was LED. TGA measurements were performed on a Pyris 1 TGA analyzer (PerkinElmer, Inc.).

Energy loss analysis

High sensitivity EQE measurements were performed using an integrated system (PECT-600, Enlitech). EL spectra and EQE$_{\mathrm{EL}}$ were performed by applying external voltage/current sources through the OPV cells (ELCT-3010, Enlitech). According to the well-developed theory,[5-6] the V_{loss} in OPV cell can be described in the follow equation

$$\Delta E_{loss} = \Delta E_{CT} + \Delta E_{rad} + \Delta E_{non-rad} \tag{S1}$$

where ΔE_{CT} is the difference between optical bandgap (E_{g}) and the charge transfer state (E_{CT}), ΔE_{rad} is the radiative energy loss, and $\Delta E_{\mathrm{non\text{-}rad}}$ is the non-radiative energy loss. E_{g} can be determined by the intersection of measured EL and sEQE spectra, and E_{CT} can be determined by the intersection of the fitting curves with **Equation S2**, **S3**, and **S4**.

$$EQE_{PV,CT}(E) = \frac{f}{E\sqrt{4\pi\lambda k_B T}}\exp\left(\frac{-\left(E_{CT} + \lambda - E\right)^2}{4\lambda k_B T}\right) \tag{S2}$$

$$EQE_{EL,CT}(E) = E\frac{f}{\sqrt{4\pi\lambda k_B T}}\exp\left(\frac{-\left(E_{CT} + \lambda - E\right)^2}{4\lambda k_B T}\right) \tag{S3}$$

$$EQE_{PV}(E) \propto EL(E)E^{-2}exp(\frac{E}{k_B T}) \tag{S4}$$

where k_B is Boltzmann's constant. E is the photon energy, and T is the temperature, and λ is the reorganization energy. ΔE_{rad} can be calculated by the following equation.[6]

$$\Delta E_{rad} =- kTln(\frac{J_{SC}h^3c^2}{fq2\pi(E_{CT} - \lambda)}) \tag{S5}$$

where h is Planck constant and c is the speed of light. $\Delta E_{non\text{-}rad}$ can be determined by **Equation S6**.

$$\Delta V_{non - rad} =- kTln(EQE_{EL}) \tag{S6}$$

Impedance measurement and DoS calculation

The dielectric constant (ε_r) of the active layers can be determined by **Equation S7**, where C_g is the geometry capacitance of the active layer measured at a reverse bias of -3 V in dark environment, L is the thickness of the active layer about 100 nm, A is the effective area of the OPV cells of 0.037 cm^2. The measured curves and the calculated ε_r values are shown in Figure S7a.

$$\varepsilon_r = \frac{C_g L}{\varepsilon_0 A} \tag{S7}$$

The DoS can be calculated form capacitance spectroscopy measured in dark environment. The frequency axis can be scaled to energy axis through the follows

$$E_\omega = kTln\left(\frac{2v_0}{\omega}\right) \tag{S8}$$

where ω is the angular frequency calculated by $\omega = 2\pi f$, v_0 is the attempt-to-escape frequency of 10^9 Hz. The trap density at energy E_ω can be acquired as

$$N_t(E_\omega) =- \frac{V_{bi}dC\ \omega}{qdd\omega kT} \tag{S9}$$

d is the thickness of the active layer and V_{bi} is the built-in voltage measured through Mott–Schottky characterization (Figure S7b).[7] Then the energy distribution can be described with Gaussian shape distribution

$$N_t(E) = \frac{N_t}{\sqrt{2\pi}\sigma}\exp\left[-\frac{(E_t - E)^2}{2\sigma^2}\right] \tag{S10}$$

Where N_t is the total density, E_t is the center of the DoS, σ is the disorder parameter.

Morphological characterizations

AFM height and phase images were collected using a Bruker Nanoscope V AF microscope. GIWAXS measurements were performed using an XEUSS SAXS/WAXS system (XENOCS, France). The samples were prepared by spin-coating the optimized blend solution onto Si substrates.

In-situ UV-vis absorption measurements

In-situ UV-vis absorption spectra were measured by an home-made systems consist a high-sensitivity CCD spectrometer (QE Pro, Ocean Insight), a tungsten halogen light source (HL-2000-FHSA, Ocean Insight), a spin coater (KW-4A), and a heating panel (C-MAG HS7, IKA).

UV-vis absorption and FT-IR absorption measurements

Steady-state absorption spectra were recorded using a Hitachi UH5300 spectrophotometer. FT-IR absorption spectra were measured by a Bruker EQUINOX55 spectrophotometer.

Femtosecond TA measurements and analyses

Femtosecond TA spectroscopy was conducted using the Helios (Ultrafast) pump-probe System in collaboration with a Regenerative Amplified Laser System (Coherent). The Ti:sapphire amplifier (Astrella, Coherent) generated an 800 nm pulse with a repetition rate of 1 kHz, a duration of 100 fs, and an energy of 7 mJ per pulse. The 800 nm pulse was then divided into two parts using a beam splitter. One part was directed into an optical parametric amplifier (TOPAS, Coherent) to produce the 800 nm pump pulses. The other part was focused onto sapphire and YAG plates, generating white light supercontinuum for the probe beams with spectra ranging from 420-800 nm and 750-1600 nm, respectively. The time delay between the pump and probe was controlled by a motorized optical delay line with a maximum delay time of 8 ns. The sample films were deposited onto 1 mm-thick quartz plates and encapsulated in epoxy resin in a nitrogen-filled glove box to mitigate the effects of water and oxygen in the air. The pump pulse was modulated by a mechanical chopper with a frequency of

500 Hz and then focused onto the mounted sample along with the probe beams. The probe beam was collimated and directed into a fiber-coupled multichannel spectrometer equipped with a CCD sensor.

The hole transfer rate and efficiency were calculated by the following equations.

$$k_{HT} = k_r - k_0 \tag{S11}$$

$$\eta_{HT} = k_{HT}/(k_{HT} + k_0) \tag{S12}$$

where k_r is the rising rate of the donor GSB signal, k_0 is the rate of eC9 GSB decay kinetics in corresponding blends (Figure S26), k_HT is the hole transfer rate, and η_HT is the hole transfer efficiency.[8] The calculation details were summarized in Table S6.

PL and TRPL measurements

The PL spectra and TRPL dynamics were obtained using a custom-designed confocal microscopy-based spectroscopy system. A Ti:sapphire amplifier (Maitai HP, Spectra Physics) was utilized to generate an 800 nm pulse with a frequency of 80 MHz and a pulse width of 35 fs. This 800 nm pulse was then directed into a frequency doubler to produce a 400 nm pulse, which was further coupled into the confocal microscopy system (Nanofinder FLEX2, Tokyo Instruments, Inc.) to excite the film specimens. The PL spectra were recorded using a fiber-connected spectrometer (DU420A-OE, ANDOR) and the TRPL kinetics were recorded using a TCSPC module (Becker & Hickl, SPC-150). The pump power density was maintained at a constant value of 5 μJ cm^{-2}. For the temperature-depended PL measurements, the sample temperature was controlled by Model 325 Cryogenic Temperature Controller (Lake Shore Cryotronics, Inc.) in a Liquid nitrogen thermostatic chamber. All samples were fabricated on quartz substrates and were enclosed in a nitrogen-filled glove box with epoxy resin. The instrument response function (IRF) is shown in Figure S25.

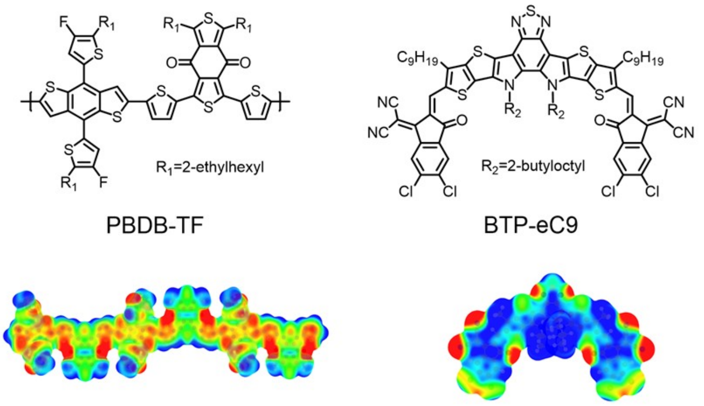

Figure S1. Molecular structures and ESP distributions of PBDB-TF and eC9.

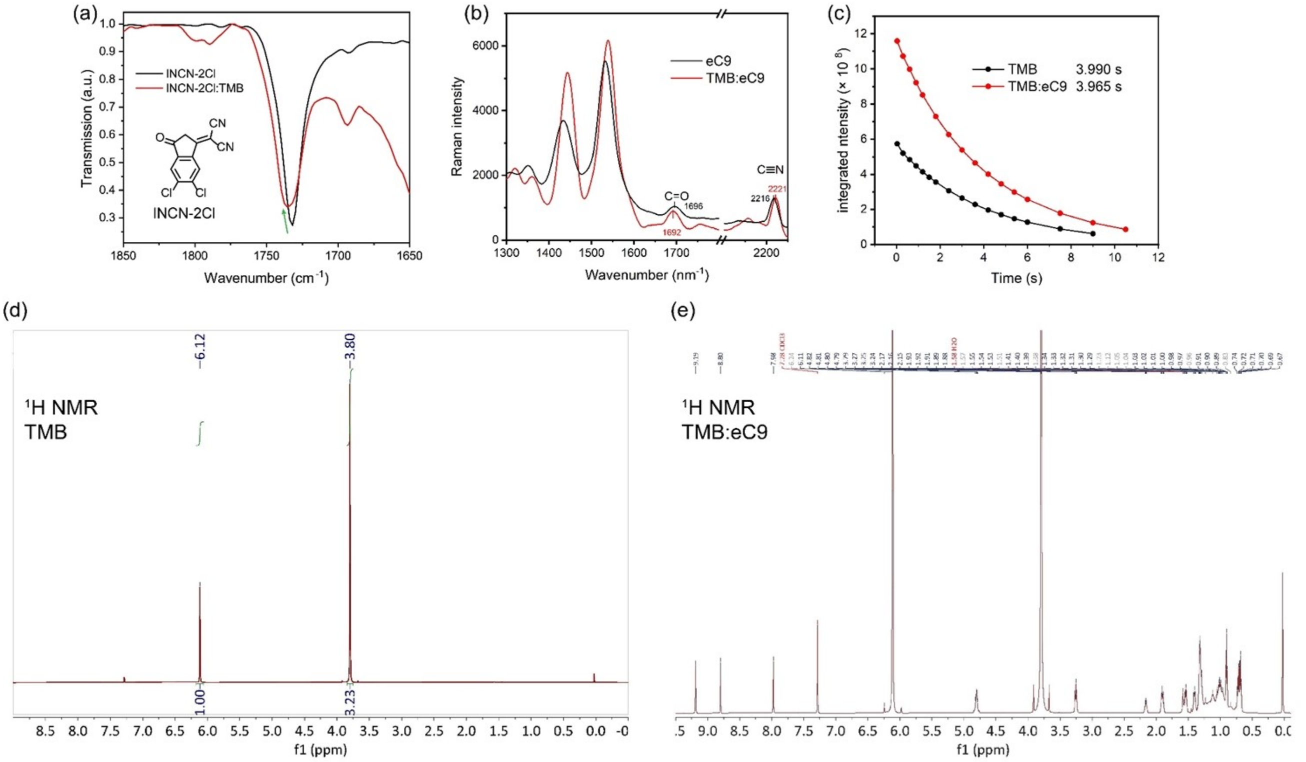

Figure S2. (a) FTIR spectra of the C=O stretching vibration of neat 2-(5,6-dichloro-3-oxo-2,3-dihydro-1H-inden-1-ylidene)malononitrile (INCN-2Cl) and INCN-2Cl:TMB blend. (b) Raman spectra of eC9 and TMB:eC9 blend. The Raman peak at 1696 cm^{-1} represents the C = O vibration, peak at 2216 cm^{-1} is the nitrile peak, the peak at 1434 cm^{-1} represents the C = C vibration of the fused thiophenes, and 1532 cm^{-1} is the alkene peak. The shifts in FTIR and Raman spectra indicate the intermolecular interaction between TMB and the edge group of eC9. (c) Curves of the experimental data of ^{1}H NMR spin-spin relaxation time (T_2) experiments on TMB and TMB:eC9 solution. The exponential function fitted relaxation times are marked. (d) ^{1}H NMR spectrum of TMB. (e) ^{1}H NMR spectrum of TMB:eC9. The peaks at 6.12 and 3.80 ppm in (d) can be assign to ^{1}H on the benzene and ^{1}H on the methyl, respectively. It shows that neat TMB process a longer T_2 time of 3.990 s, while the T_2 value decreases to 3.965 s in TMB:eC9 blend. This result provides further evidence of the intermolecular interaction between TMB and eC9.

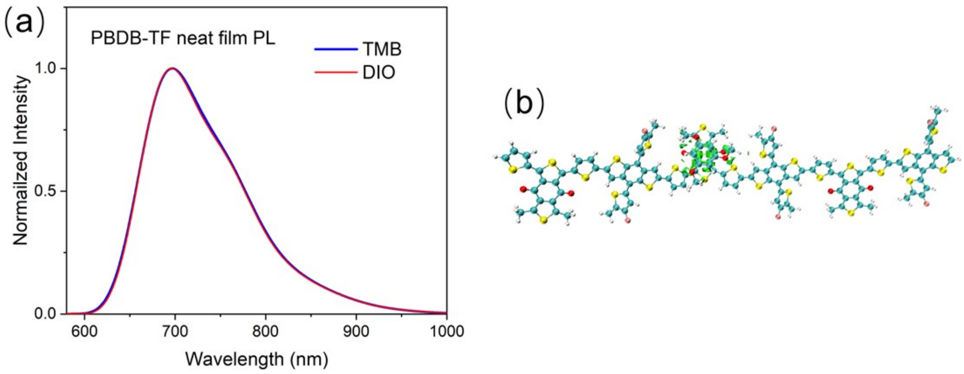

Figure S3. (a) PL spectra of PBDB-TF films processed with DIO and TMB as additives. (b) Optimized packing configuration between eC9 and TMB molecules and the intermolecular interaction distribution through the method of independent gradient model based on Hirshfeld partition.

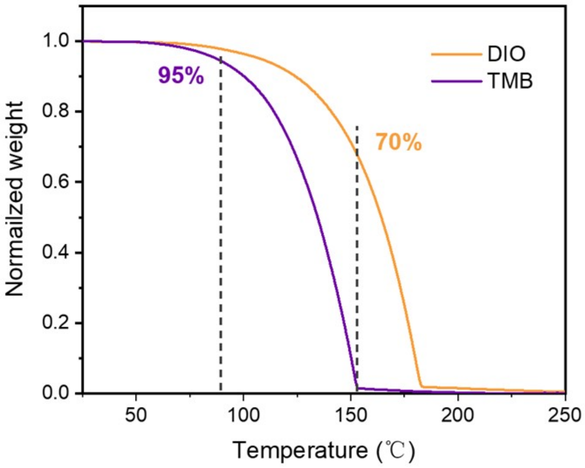

Figure S4. TGA plot of TMB and DIO at a scan rate of 10 °C min^{-1} under nitrogen atmosphere.

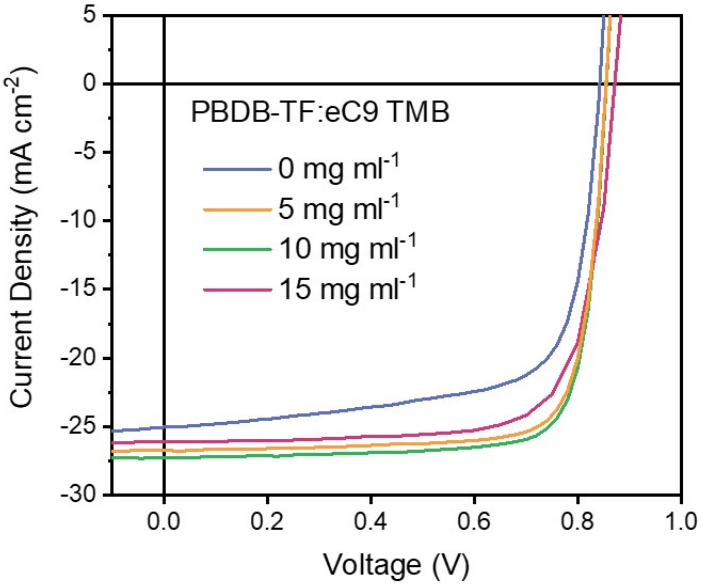

Figure S5. The *J-V* curves of the PBDB-TF:eC9 cells treated with different TMB concentration.

Table S1. The photovoltaic parameters for PBDB-TF:eC9 cells treated with different TMB concentration.

TMB concentration	V_{OC} [V]	J_{SC} [mA cm^{-2}]	FF [%]	PCE^a [%]
0 mg ml^{-1}	0.840	25.06	70.80	14.90 (14.36±0.28)
5 mg ml^{-1}	0.851	26.73	79.55	18.10 (17.99±0.10)
10 mg ml^{-1}	0.854	27.26	79.95	18.61 (18.46±0.15)
15 mg ml^{-1}	0.862	26.12	74.31	16.73 (16.46±0.29)

[a] Averaged PCE of five devices

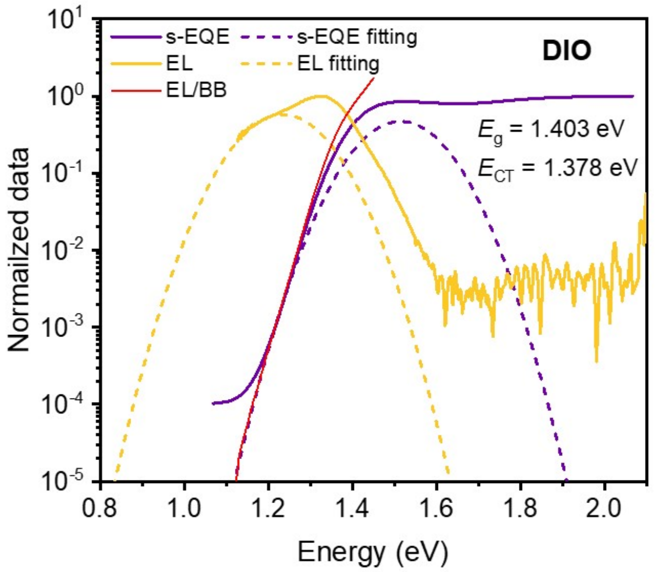

Figure S6. EL and sEQE spectra of DIO-processed OPV cells.

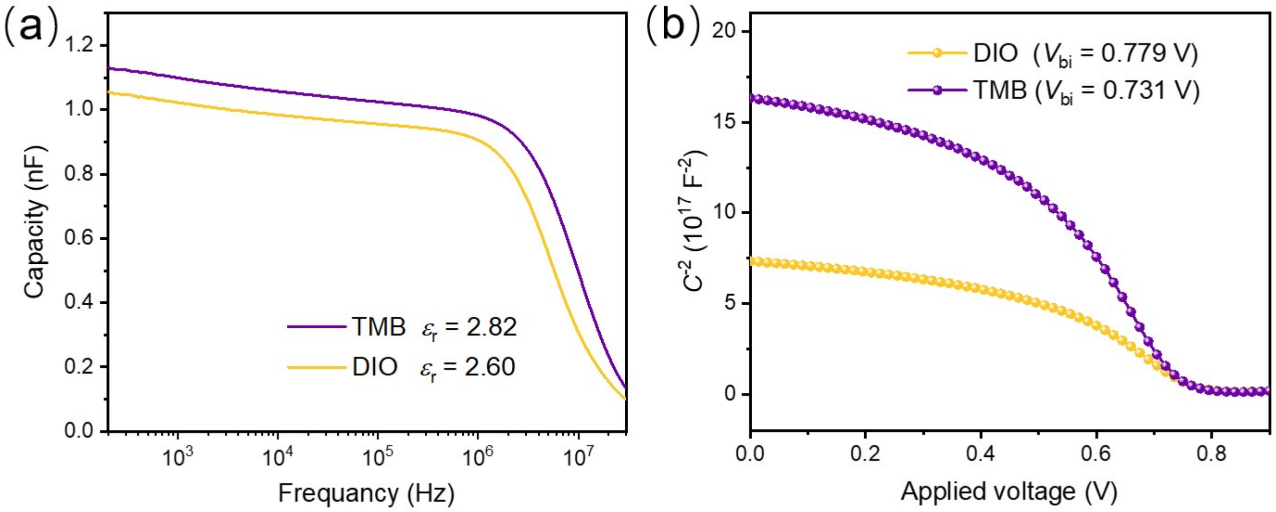

Figure S7. (a) Capacitance-frequency characteristics of PBDB-TF:eC9 cells treated by DIO and TMB under dark. The dielectric constant (ε^r) is 2.82 and 2.60 for DIO- and TMB- treated cells, respectively. (b) Built-in potential (V_{bi}) of the OPV cells measured following the Mott-Schottky method.

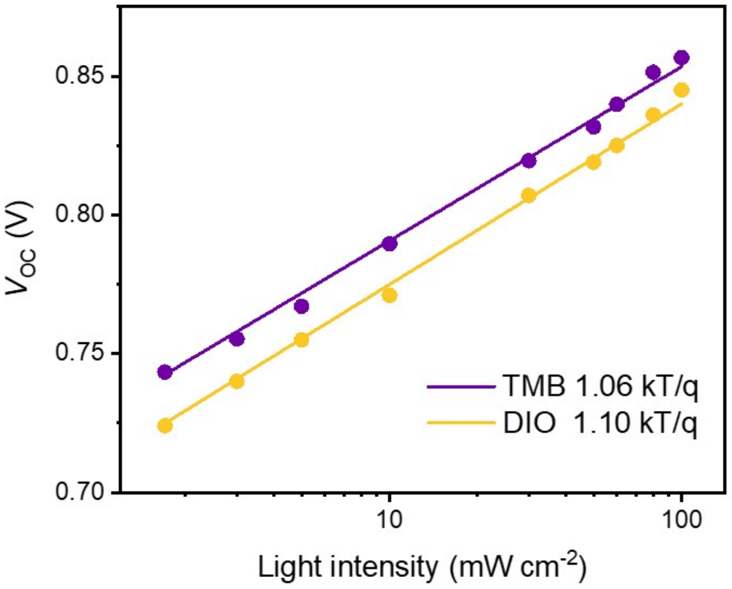

Figure S8. V_{OC} depends on the incident light intensity of DIO- and TMB- treated cells.

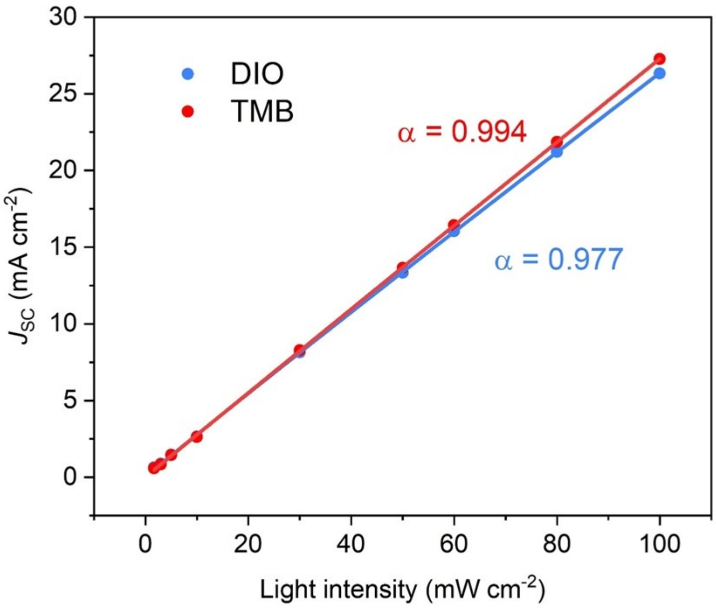

Figure S9. J_{SC} depends on the incident light intensity of DIO- and TMB-treated devices.

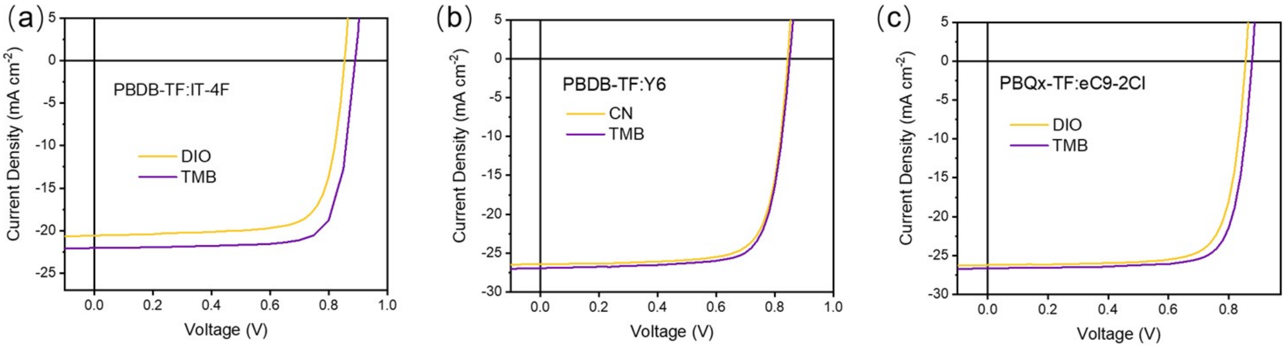

Figure S10. The *J-V* curves of the OPV cells treated by different additives. (a) PBDB-TF:IT-4F, (b) PBDB-TF:Y6, (c) PBQx-TF:eC9-2Cl

Table S2. The photovoltaic parameters for PBDB-TF: IT-4F, PBDB-TF:Y6, and PBQx-TF:eC9-2Cl OPV cells treated by different additives.

Active layer	V_{OC} [V]	J_{SC} [mA cm^{-2}]	FF [%]	PCE[a] [%]
PBDB-TF: IT-4F DIO	0.851	20.57	75.88	13.28 (13.09±0.19)
PBDB-TF: IT-4F TMB	0.878	22.04	77.99	15.09 (15.05±0.13)
PBDB-TF:Y6 CN	0.842	25.87	75.91	16.53 (16.32±0.20)
PBDB-TF:Y6 TMB	0.851	26.96	76.43	17.53 (17.23±0.32)
PBQx-TF:eC9-2Cl DIO	0.854	26.25	77.10	17.28 (17.08±0.18)
PBQx-TF:eC9-2Cl TMB	0.875	26.65	78.27	18.25 (18.07±0.18)

[a] Averaged PCE of five devices

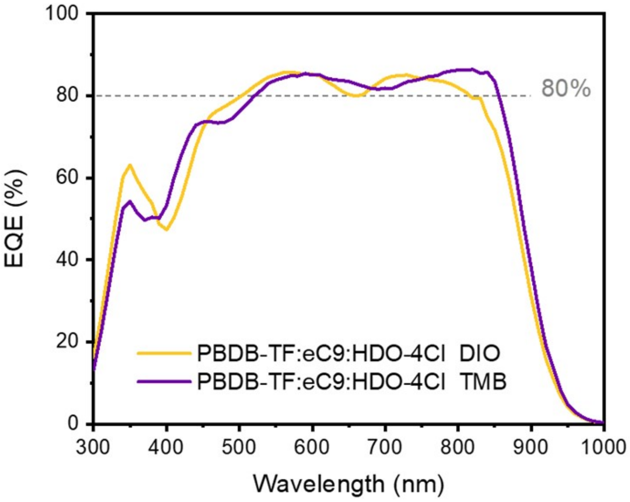

Figure S11. EQE spectra of the DIO- and TMB-processed PBDB-TF:eC9:HDO-4Cl ternary OPV cells.

Table S3. The summarization of photovoltaic parameters of OSCs fabricated with volatile solid additives.

additives	photoactive layers	V_{OC} [V]	J_{SC} [mA cm^{-2}]	J_{cal} [mA cm^{-2}]	FF [%]	PCE [%]
1,3,5-Trimethoxybenzene (this work)	PBDB-TF:eC9:HDO-4Cl	0.883	27.27	26.92	80.17	19.30
3,5-dichlorobromobenzene[9]	PBQx-TF:eC9-2Cl	0.879	27.2	26.4	80.4	19.2
1,3,5-Trichlorobenzene[10]	PBDB-TF:eC9	0.861	27.88	\	80.39	19.31
1,3-dibromo-5-chlorobenzene[11]	PBDB-TF:L8-BO	0.89	25.9	25.2	80.2	18.5
1,2-dibromobenzene[12]	D18-Cl:N3	0.856	26.99	25.66	80.2	18.54
1,4-diiodobenzene[13]	PBDB-TF:Y6:ICBA	0.84	26.5	26.27	79.62	17.72
1,4-diiodobenzene[14]	D18-Cl:L8-BO	0.922	26.6	25.0	75.6	18.7
SAD2[15]	PBDB-TF:L8-BO	0.889	26.73	25.43	79.32	18.85

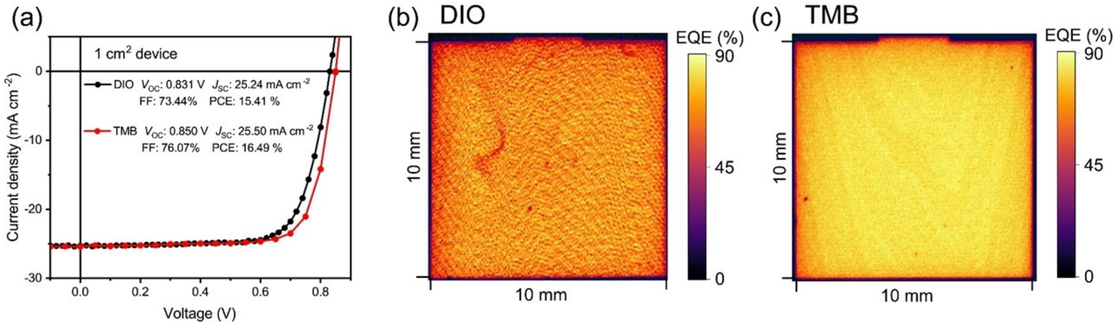

Figure S12. (a) *J-V* curves of blade-coated PBDB-TF:eC9 OSCs (effective area of 1 cm^2) with DIO and TMB incorporated as additives. (b) and (c) are the EQE mapping images (at 520 nm) of the corresponding blade-coated devices.

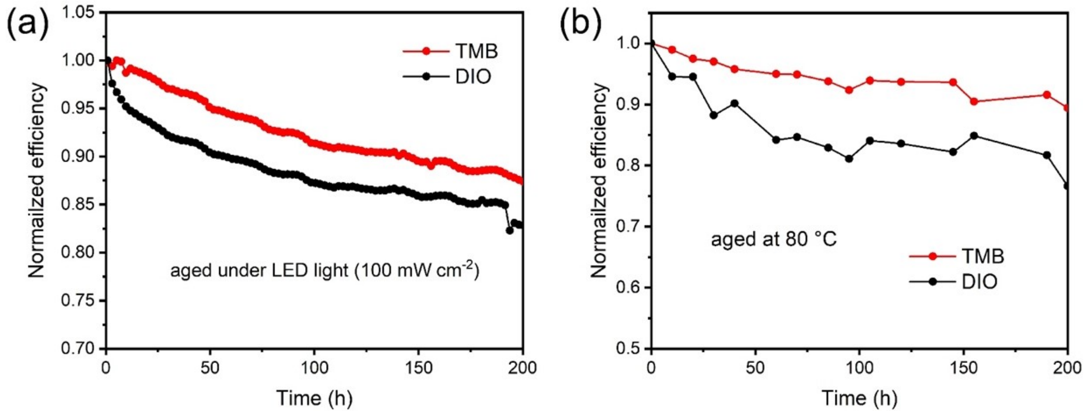

Figure S13. (a) Photostability and (b) thermostability of DIO- and TMB-treated PBDB-TF:eC9 OSCs.

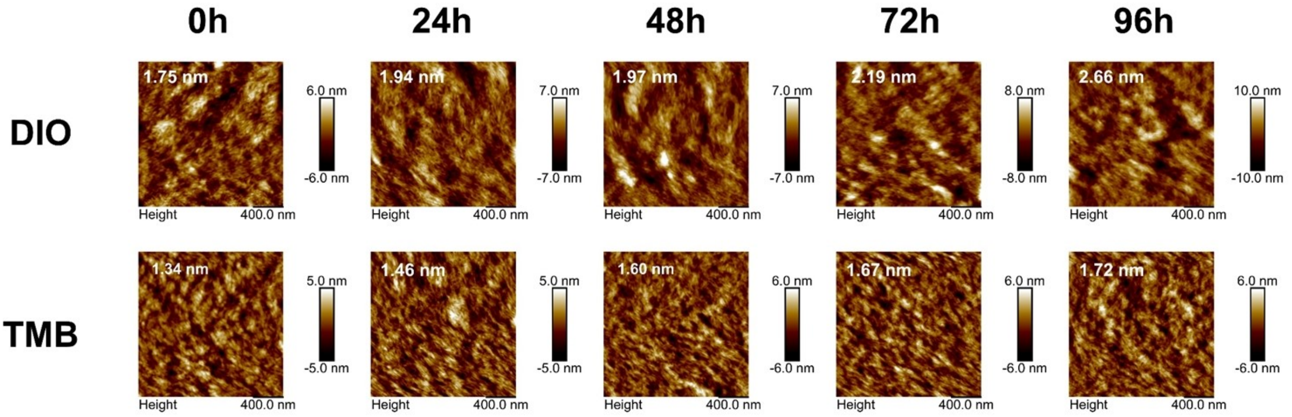

Figure S14. AFM height images of DIO- and TMB-treated PBDB-TF:eC9 films aged under LED light (100 mW cm^{-2}) for different times. R_q values are marked on the images.

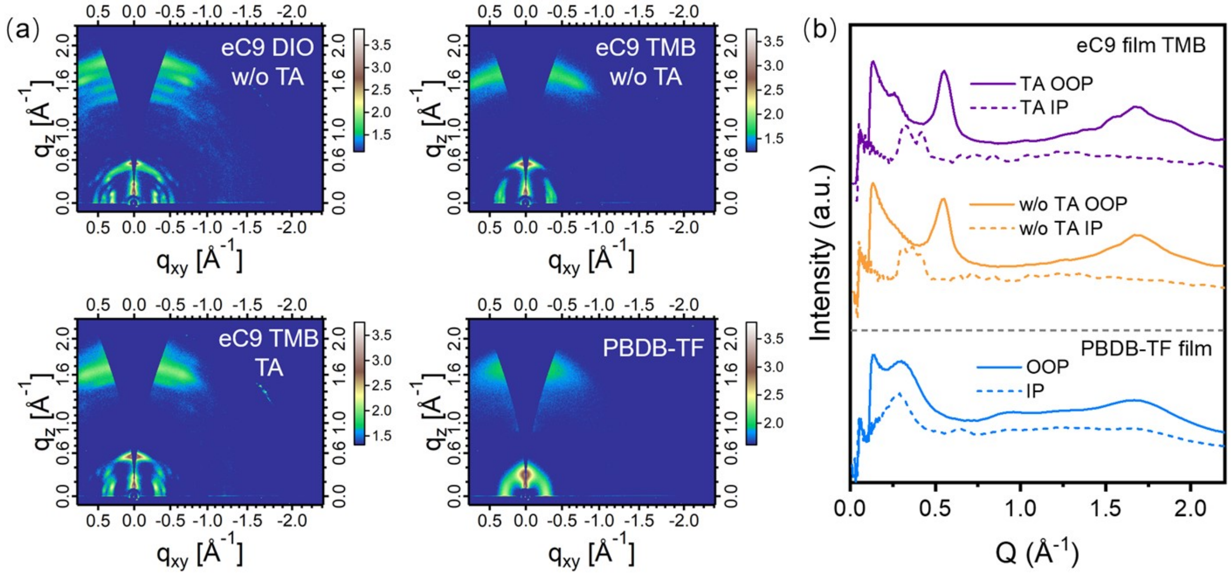

Figure S15. (a) 2D-GIWAXS patterns of DIO-treated eC9 neat film without thermal annealing, TMB-treated eC9 neat films with and without thermal annealing, and PBDB-TF neat film without additive. (b) Line-cut profiles along IP and OOP direction of the corresponding films.

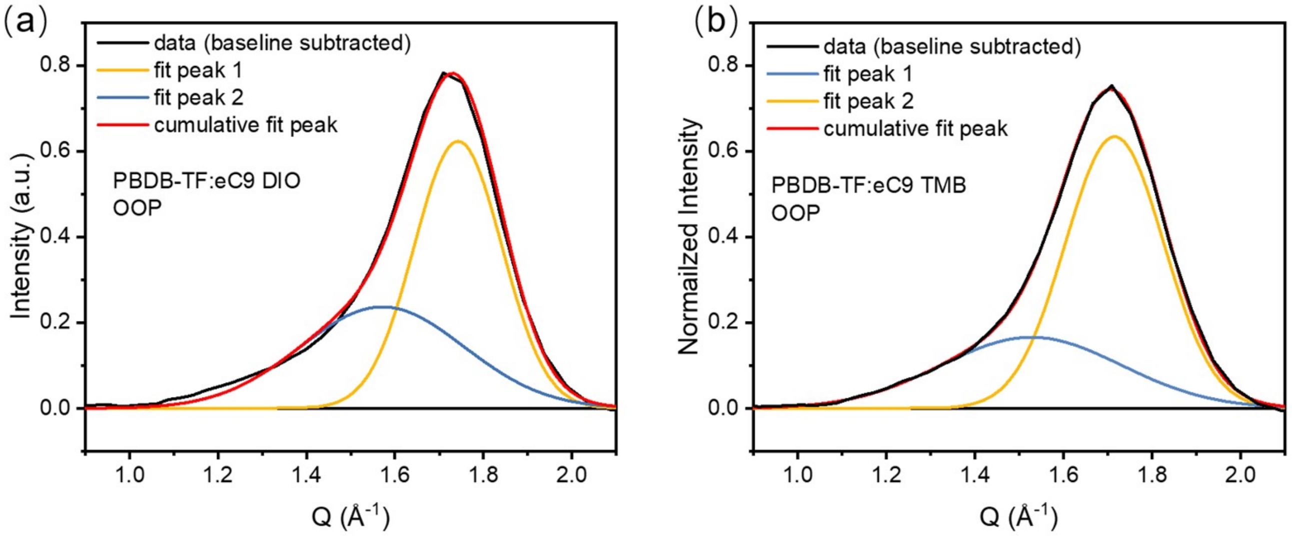

Figure S16. The fitting curves of the GIWAXS line-cut profiles of the blend films along OOP direction.

Table S4. Structure parameters of the (010) peak for DIO- and TMB-treated films obtained from GIWAXS data.

Active layer	Q [Å^{-1}]	d-spacing [Å]	FWHM [Å^{-1}]	CCL [Å]
PBDB-TF:eC9 DIO	1.74	3.60	0.262	23.96
PBDB-TF:eC9 TMB	1.69	3.71	0.233	26.95

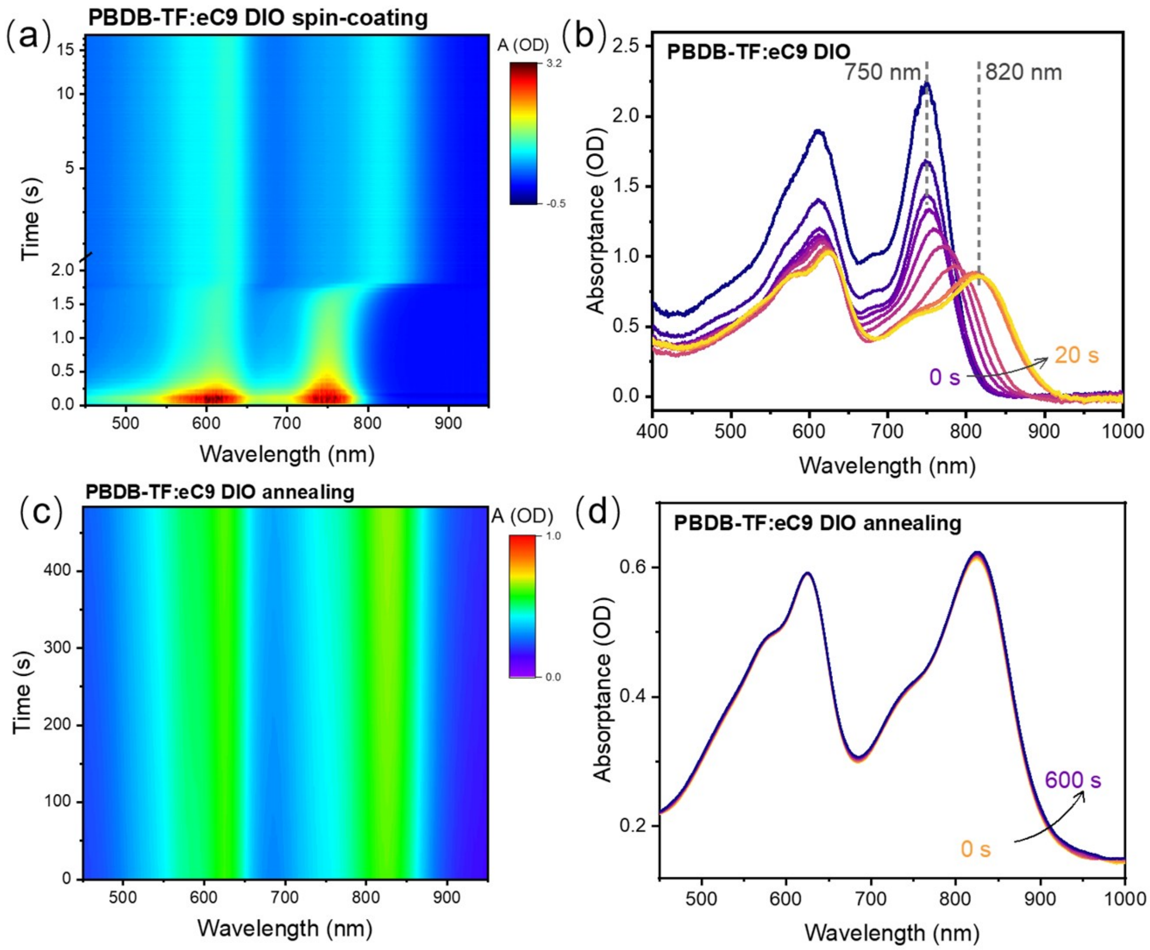

Figure S17. (a) *In situ* 2D UV-visible absorption profile and (b) *in situ* UV-visible absorption spectra of DIO-incorporated PBDB-TF:eC9 blend during the spin-coating process. (c) *In situ* 2D UV-visible absorption profile and (d) *in situ* UV-visible absorption spectra of TMB-incorporated PBDB-TF:eC9 blend during the thermal annealing process.

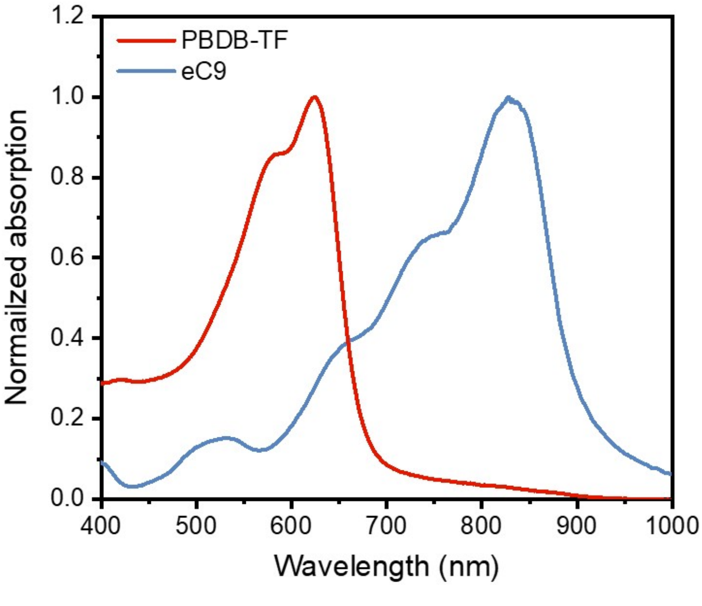

Figure S18. Normalized absorption spectra of neat PBDB-TF and eC9 films.

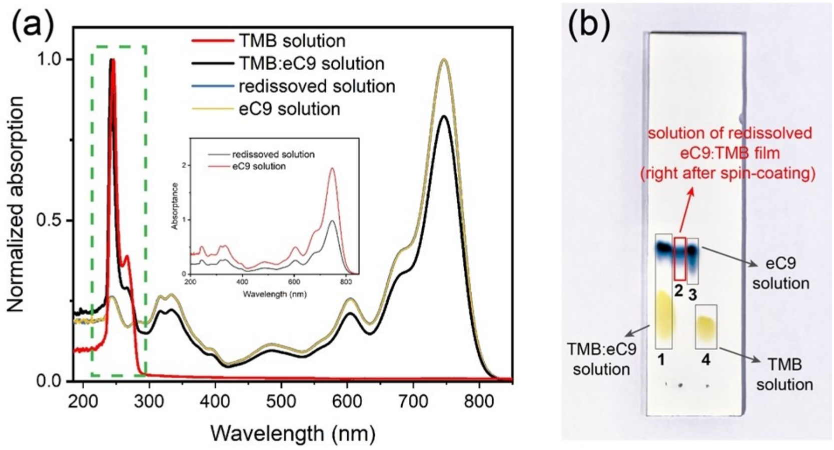

Figure S19. (a) UV-visible absorption spectra of TMB solution, eC9 solution, TMB:eC9 solution, and the solution of redissolved eC9:TMB film (right after spin-coating). Inset shows the measure spectra for clear distinction. The solvent is chloroform. (b) Picture of the TLC plate. Spot 1, TMB:eC9 solution; Spot 2, solution of redissolved eC9:TMB film (right after spin-coating, the origin molar ratio of eC9:TMB is 1:1); Spot 3, neat eC9 solution; Spot 4, neat TMB solution.

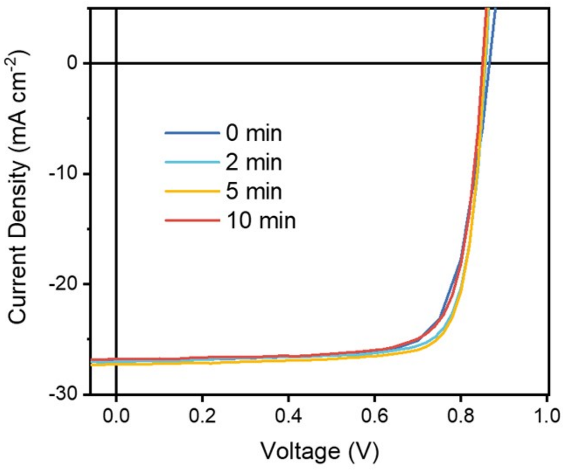

Figure S20. *J-V* curves of the TMB-treated PBDB-TF:eC9 OPV cells annealed at different temperatures

Table S5. The photovoltaic parameters for TMB-treated PBDB-TF:eC9 annealed at different temperatures

Annealing time	V_{OC} [V]	J_{SC} [mA cm^{-2}]	FF [%]	PCE [%]
0 min	0.860	26.96	74.45	17.46 (17.33±0.15)
2 min	0.857	27.03	78.84	18.34 (18.06±0.17)
5 min	0.854	27.26	79.95	18.61 (18.46±0.15)
10 min	0.847	26.79	77.35	17.56 (17.48±0.11)

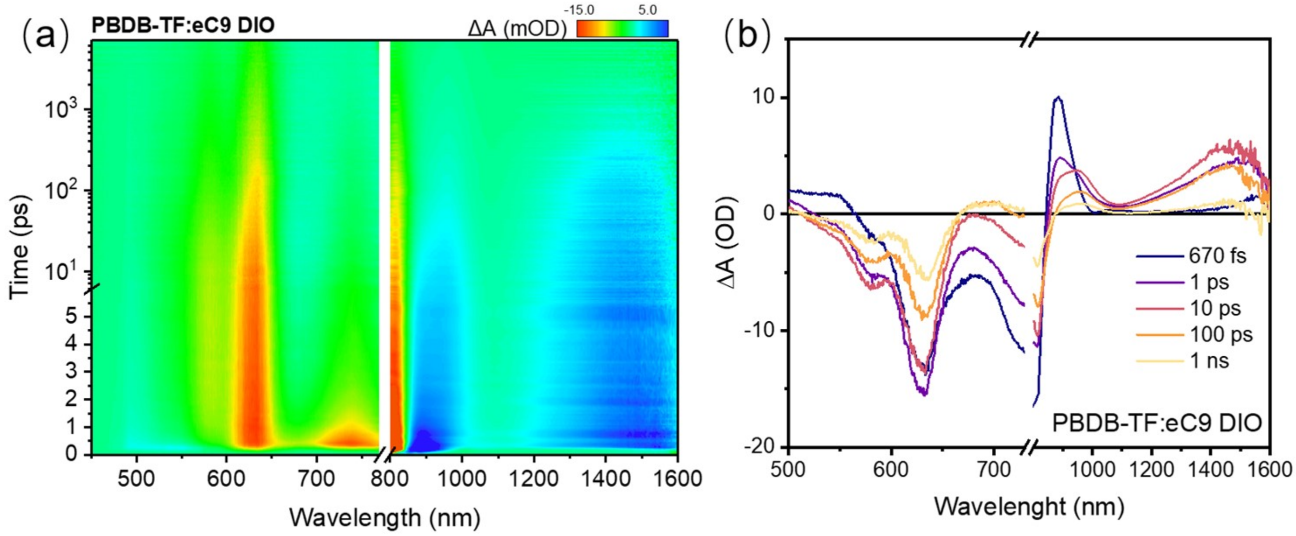

Figure S21. The (a) 2D TA profile and (b) TA spectra at different time delays of DIO-treated PBDB-TF:eC9 film pumped at 800 nm.

Table S6. Fitting results of the hole-transfer dynamics probed at 580 nm in TA spectra.

Films	t_r [ps]	k_r [ps^{-1}]	t_0 [ps]	k_0 [ps^{-1}]	k_{HT} [ps^{-1}]	η_{HT} [%]
PBDB-TF:eC9 DIO	0.42	2.38	5.89	0.17	2.21	92.8
PBDB-TF:eC9 TMB	0.31	3.22	5.34	0.18	3.04	94.4

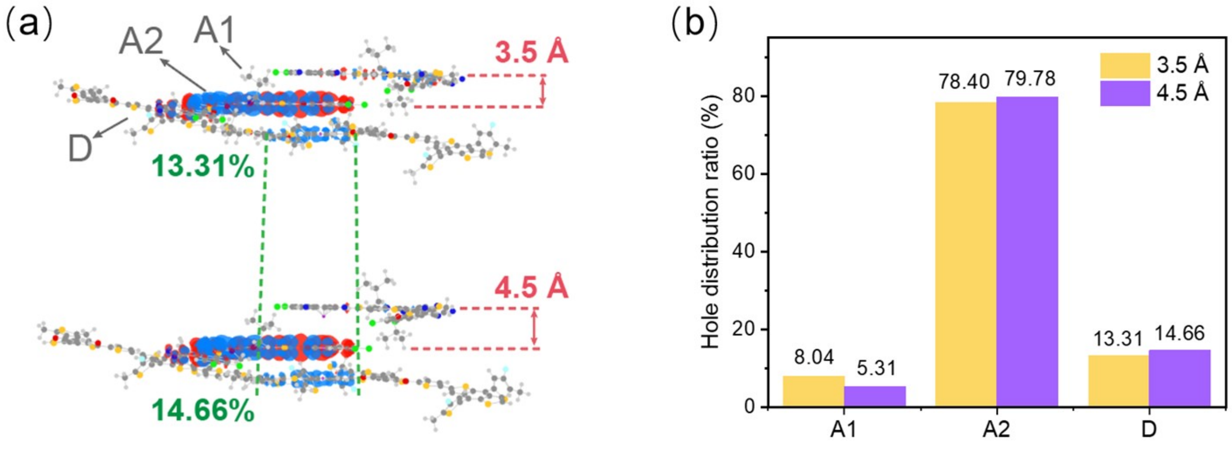

Figure S22. (a) Charge transfer features between PBDB-TF and eC9 dimers with different packing distances. PBDB-TF and eC9 molecules are marked as D, A1, and A2, respectively. The red dot lines mark the packing distances of dimers and the green dot lines compare the hole distributions on PBDB-TF molecules. (b) Details of hole distribution ratios on each component.

Table S7. Fitting results of the DLE dynamics probed at 1500 nm in TA spectra.

Films	t_1 [ps]	A_1 [%]	t_2 [ps]	A_2 [%]
PBDB-TF:eC9 DIO	13.4	38.6	739.3	61.4
PBDB-TF:eC9 TMB	4.0	52.7	745.2	47.3

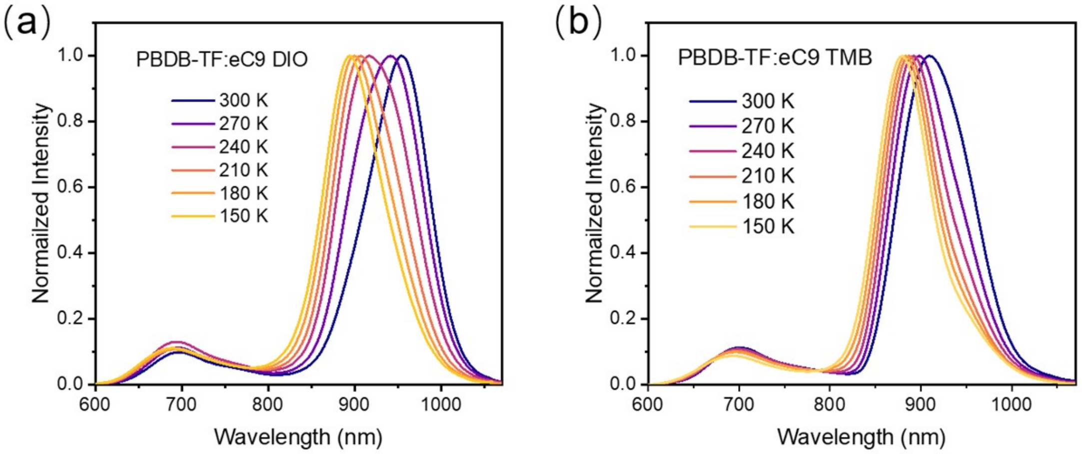

Figure S23. The temperature-depended PL spectra of (a) DIO- and (b) TMB-treated PBDB-TF:eC9 blend films

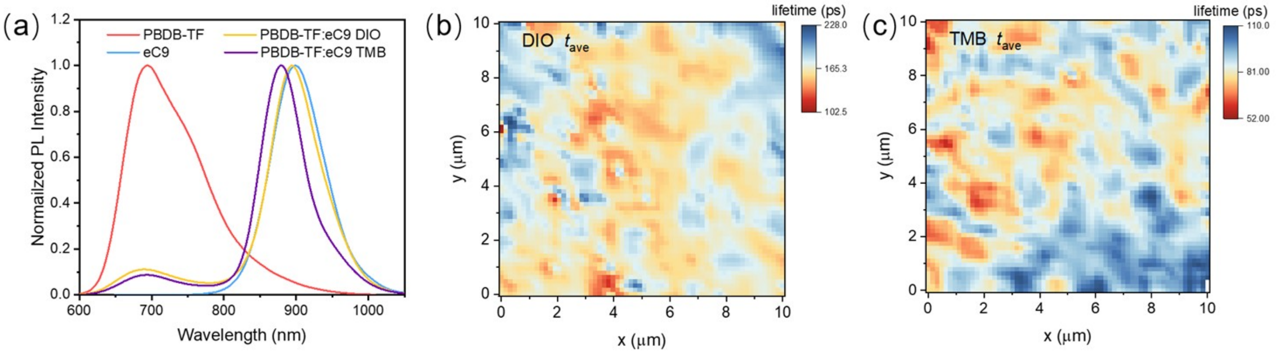

Figure S24. (a) PL spectra of PBDB-TF and eC9 neat films, and PBDB-TF:eC9 blend films treated by DIO and TMB additives. (b) and (c) are the TRPL mapping images of DIO- and TMB-treated PBDB-TF:eC9 blend films, respectively, excited by 400 nm pump and probe at 900 nm. The PL lifetime is fitted by the double-exponential decay function. The mapping area is 10 µm^2 and the mapping density is 64 × 64.

Table S8. Fitting results of the TRPL dynamics probed at 900 nm.

Films	t_1 [ps]	A_1 [%]	t_2 [ps]	A_2 [%]	t_{ave} [ps]
PBDB-TF:eC9 DIO	114.2	73.0	268.3	27.0	155.8
PBDB-TF:eC9 TMB	72.7	97.5	405.6	2.5	81.0

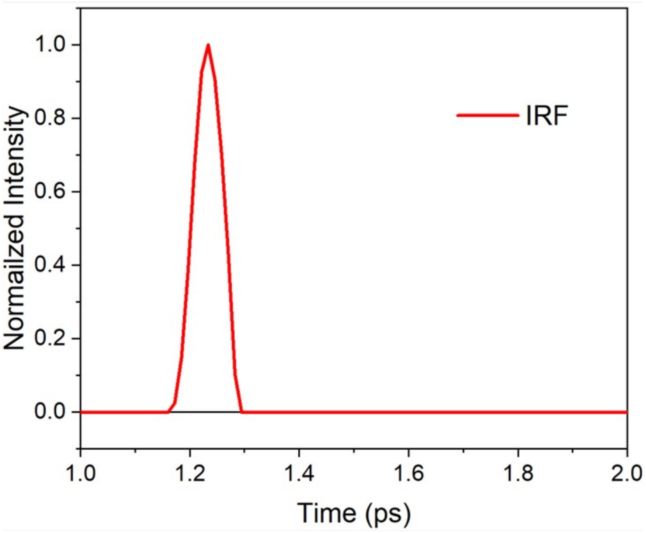

Figure S25. IRF of the TRPL setup.

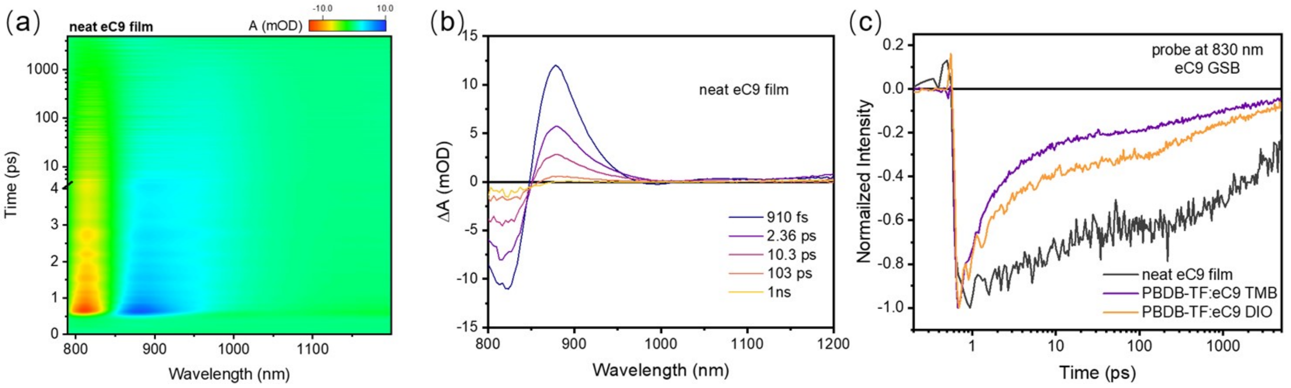

Figure S26. (a) 2D TA profile and (b) TA spectra at different time delays of neat eC9 film pumped at 800 nm. (c) eC9 GSB dynamics in neat film, TMB-treated blend film, and DIO-treated blend film.

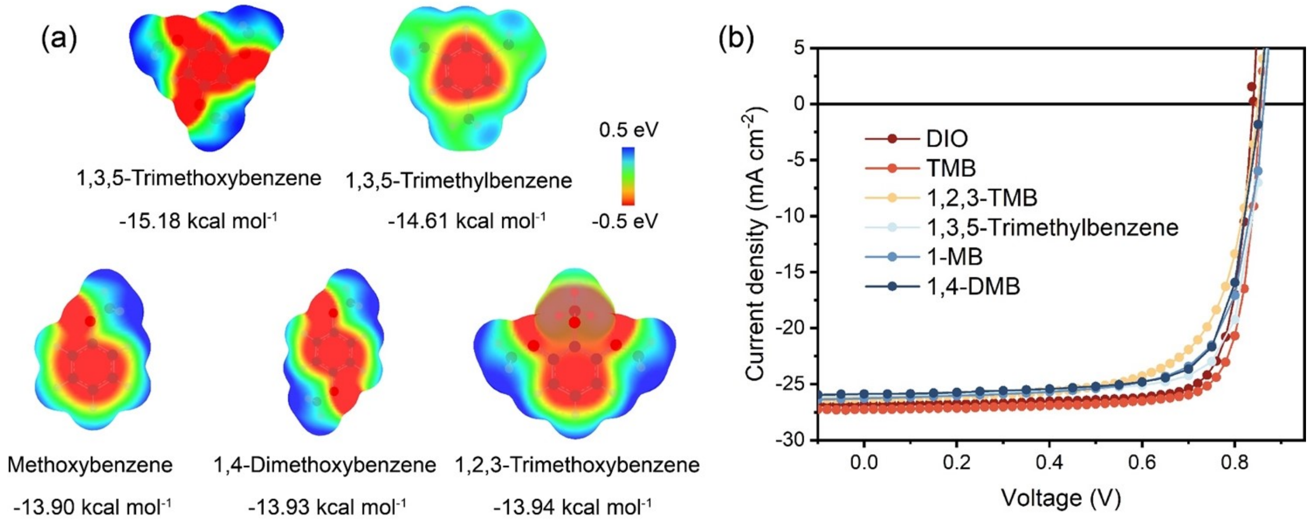

Figure S27. (a) ESP distributions and average ESP values of the center benzene of TMB, 1,3,5-trimethylbenzene, methoxybenzene, 1,4-dimethoxybenzene, and 1,2,3-trimethoxybenzene. (b) *J-V* curves of the PBDB-TF:eC9 OSCs with corresponding additives.

Table S9. The photovoltaic parameters for PBDB-TF:eC9 OSCs with different additives.

Additive	V_{OC} [V]	J_{SC} [mA cm^{-2}]	FF [%]	PCE[a)] [%]
DIO	0.837	26.44	79.38	17.57 (17.50±0.06)
TMB	0.854	27.26	79.95	18.61 (18.46±0.15)
1,3,5-Trimethylbenzene	0.851	26.41	75.89	17.06 (16.93±0.14)
Methoxybenzene	0.853	26.33	72.11	16.20 (16.03±0.20)
1,4-Dimethoxybenzene	0.844	26.28	74.46	16.52 (16.27±0.23)
1,2,3-Trimethoxybenzene	0.847	26.53	68.92	15.49 (15.21±0.25)

[a)] Averaged PCE of five devices

References

[1] M. J. Frisch, G. W. Trucks, H. B. Schlegel, G. E. Scuseria, M. A. Robb, J. R. Cheeseman, G. Scalmani, V. Barone, B. Mennucci, G. A. Petersson, H. Nakatsuji, M. Caricato, X. Li, H. P. Hratchian, A. F. Izmaylov, J. Bloino, G. Zheng, J. L. Sonnenberg, M. Hada, M. Ehara, K. Toyota, R. Fukuda, J. Hasegawa, M. Ishida, T. Nakajima, Y. Honda, O. Kitao, H. Nakai, T. Vreven, J. A. Montgomery Jr., J. E. Peralta, F. Ogliaro, M. J. Bearpark, J. Heyd, E. N. Brothers, K. N. Kudin, V. N. Staroverov, R. Kobayashi, J. Normand, K. Raghavachari, A. P. Rendell, J. C. Burant, S. S. Iyengar, J. Tomasi, M. Cossi, N. Rega, N. J. Millam, M. Klene, J. E. Knox, J. B. Cross, V. Bakken, C. Adamo, J. Jaramillo, R. Gomperts, R. E. Stratmann, O. Yazyev, A. J. Austin, R. Cammi, C. Pomelli, J. W. Ochterski, R. L. Martin, K. Morokuma, V. G. Zakrzewski, G. A. Voth, P. Salvador, J. J. Dannenberg, S. Dapprich, A. D. Daniels, Ö. Farkas, J. B. Foresman, J. V. Ortiz, J. Cioslowski, D. J. Fox, Gaussian, Inc., Wallingford, CT, USA 2009.

[2] Z. Liu, T. Lu, Q. Chen, *Carbon* **2020**, 165, 468.

[3] T. Lu, Q. Chen, *J Comput Chem* **2022**, 43, 539.

[4] T. Lu, F. Chen, *J Comput Chem* **2012**, 33, 580.

[5] J. Yao, T. Kirchartz, M. S. Vezie, M. A. Faist, W. Gong, Z. He, H. Wu, J. Troughton, T. Watson, D. Bryant, J. Nelson, *Physical Review Applied* **2015**, 4.

[6] A. Karki, J. Vollbrecht, A. L. Dixon, N. Schopp, M. Schrock, G. N. M. Reddy, T. Q. Nguyen, *Adv. Mater.* **2019**, 31, 1903868.

[7] S. Khelifi, K. Decock, J. Lauwaert, H. Vrielinck, D. Spoltore, F. Piersimoni, J. Manca, A. Belghachi, M. Burgelman, *J. Appl. Phys.* **2011**, 110.

[8] G. Zhou, M. Zhang, Z. Chen, J. Zhang, L. Zhan, S. Li, L. Zhu, Z. Wang, X. Zhu, H. Chen, L. Wang, F. Liu, H. Zhu, *ACS Energy Lett.* **2021**, 6, 2971.

[9] J. Wang, Y. Wang, P. Bi, Z. Chen, J. Qiao, J. Li, W. Wang, Z. Zheng, S. Zhang, X. Hao, J. Hou, *Adv. Mater.* **2023**, Accepted Articles.

[10] J. Fu, P. W. K. Fong, H. Liu, C.-S. Huang, X. Lu, S. Lu, M. Abdelsamie, T. Kodalle, C. M. Sutter-Fella, Y. Yang, G. Li, *Nat. Commun.* **2023**, 14, 1760.

[11] X. Song, K. Zhang, R. Guo, K. Sun, Z. Zhou, S. Huang, L. Huber, M. Reus, J. Zhou, M. Schwartzkopf, S. V. Roth, W. Liu, Y. Liu, W. Zhu, P. Muller-Buschbaum, *Adv. Mater.* **2022**, 34, e2200907.

[12] X. He, C. C. S. Chan, X. Zou, S. Zhang, P. W. K. Fong, J. Kim, G. Li, X. Hu, W. Ma, K. S. Wong, W. C. H. Choy, *Adv. Energy Mater.* **2023**, 13.

[13] J. Fu, H. Chen, P. Huang, Q. Yu, H. Tang, S. Chen, S. Jung, K. Sun, C. Yang, S. Lu, Z. Kan, Z. Xiao, G. Li, *Nano Energy* **2021**, 84, 105862.

[14] G. Cai, Z. Chen, X. Xia, Y. Li, J. Wang, H. Liu, P. Sun, C. Li, R. Ma, Y. Zhou, W. Chi, J. Zhang, H. Zhu, J. Xu, H. Yan, X. Zhan, X. Lu, *Adv Sci* **2022**, 9, e2200578.

[15] C. Li, X. Gu, Z. Chen, X. Han, N. Yu, Y. Wei, J. Gao, H. Chen, M. Zhang, A. Wang, J. Zhang, Z. Wei, Q. Peng, Z. Tang, X. Hao, X. Zhang, H. Huang, *J Am Chem Soc* **2022**, 144, 14731.